

Quantitative 2D and 3D Phase Contrast MRI: Optimized Analysis of Blood Flow and Vessel Wall Parameters

A.F. Stalder,^{1*} M.F. Russe,² A. Frydrychowicz,² J. Bock,¹ J. Hennig,¹ and M. Markl¹

Quantification of CINE phase contrast (PC)-MRI data is a challenging task because of the limited spatiotemporal resolution and signal-to-noise ratio (SNR). The method presented in this work combines B-spline interpolation and Green's theorem to provide optimized quantification of blood flow and vessel wall parameters. The B-spline model provided optimal derivatives of the measured three-directional blood velocities onto the vessel contour, as required for vectorial wall shear stress (WSS) computation. Eight planes distributed along the entire thoracic aorta were evaluated in a 19-volunteer study using both high-spatiotemporal-resolution planar two-dimensional (2D)-CINE-PC ($\sim 1.4 \times 1.4 \text{ mm}^2/24.4 \text{ ms}$) and lower-resolution 3D-CINE-PC ($\sim 2.8 \times 1.6 \times 3 \text{ mm}^3/48.6 \text{ ms}$) with three-directional velocity encoding. Synthetic data, error propagation, and inter-individual, intermodality, and interobserver variability were used to evaluate the reliability and reproducibility of the method. While the impact of MR measurement noise was only minor, the limited resolution of PC-MRI introduced systematic WSS underestimations. In vivo data demonstrated close agreement for flow and WSS between 2D- and 3D-CINE-PC as well as observers, and confirmed the reliability of the method. WSS analysis along the aorta revealed the presence of a circumferential WSS component accounting for 10–20%. Initial results in a patient with atherosclerosis suggest the potential of the method for understanding the formation and progression of cardiovascular diseases. Magn Reson Med 60:1218–1231, 2008. © 2008 Wiley-Liss, Inc.

Key words: phase-contrast MRI (PC-MRI); wall shear stress (WSS); flow quantification; B-spline; aorta hemodynamics

The functional evaluation of the cardiovascular system is already part of the clinical routine and is expected to gain increased importance (1). Volumetric blood flow is an important estimator of the cardiovascular function in the presence of stenosis, aortic regurgitation (2), or congenital defects (3). In addition, the measurement of local flow profiles can provide important derived flow or vessel wall parameters such as the pressure difference, peak velocity, pulsatility index, and wall shear stress (WSS). WSS, the friction force of the flowing blood at the arterial wall, affects the function of endothelial cells (4–6) and the development of atherosclerosis (4,7–10) and aneurysms (11).

To assess cardiovascular function in vivo, blood flow velocity can be measured using Doppler ultrasound (US) or flow-sensitive MRI. Although Doppler US offers high spatiotemporal resolution, it is hampered by its user dependency, limited insonation angles (12), and unidirectional velocity encoding. The intrinsic sensitivity of MR to flow offers the possibility of analyzing vascular hemodynamics without restrictions to anatomic coverage or flow directions.

In this context, an alternative approach is provided by computational fluid dynamics (CFD) models with realistic boundary conditions (i.e., vascular geometry and inflow provided by CT, MRI, or US) and has already been used (11,13–15). However, it is still debated how restricting assumptions on blood rheology, vessel properties, or blood-vessel interactions may affect the accuracy of the results.

WSS depends on the spatial velocity gradient at the vessel wall and can therefore be calculated from the measured velocity fields. Considering the three-dimensional (3D) nature of blood flow, WSS is a vector quantity ($\vec{\tau}$) that can be expressed in N/m^2 . However, deriving WSS from the discrete PC-MR velocity data remains challenging. Limited spatial resolution, partial volume effects, and numerical derivation of the velocity field are likely to introduce underestimations in WSS. Nevertheless, the definition of suitable WSS estimators of WSS patterns is of high interest. Although WSS may be systematically underestimated, the results may still be sufficient to characterize normal and pathological spatiotemporal variations of WSS. Note that in this work, the term “WSS” is used to describe WSS estimations based on the interpolation of local velocity derivatives.

Although previous in vivo MR studies provided insights into the relationship between WSS and flow (10,16,17), the reported WSS values were limited to the mean axial WSS, i.e., projection of the WSS vector along the lumen direction. No comprehensive or circumferential assessment of localized WSS vector components along the vessel wall has been presented to date. WSS estimations are often simply calculated assuming a global axial parabolic velocity profile. The WSS ($\vec{\tau}$) is then oriented along the axial

direction only, and WSS simplifies to $\tau = \|\vec{\tau}\| = -\frac{4\eta Q}{\pi a^3}$ (with a = vessel radius, Q = flow and η = dynamic viscosity). However, this simplification is only valid for constant laminar flow in a straight tube.

In the 3D paraboloid method (18), axial parabolic flow profiles are assumed in sectors near the vessel wall in order to compute axial WSS. The method requires only minor user input and provides excellent repeatability, but its applicability is restricted to small or medium-sized elliptical vessels by its assumption of axial-only and pa-

¹Department of Diagnostic Radiology, Medical Physics, University Hospital Freiburg, Freiburg, Germany.

²Department of Diagnostic Radiology, University Hospital Freiburg, Freiburg, Germany.

Presented in part at the ISMRM Flow and Motion Workshop, New York, NY, 2006; 15th Annual Meeting of ISMRM, Berlin, Germany, 2007; and 16th Annual Meeting of ISMRM, Toronto, Ontario, Canada, 2008.

*Correspondence to: Aurélien Stalder, Dept. of Diagnostic Radiology, Medical Physics, Hugstetterstr. 55, D-79106 Freiburg, Germany. E-mail: aurelien.stalder@uniklinik-freiburg.de

Received 5 November 2007; revised 5 June 2008; accepted 10 July 2008.

DOI 10.1002/mrm.21778

Published online in Wiley InterScience (www.interscience.wiley.com).

© 2008 Wiley-Liss, Inc.

paraboloid flow (19). Recently, a more general method based on Lagrange polynomial interpolation of through-plane MR velocities was introduced to compute axial WSS for large arteries (20).

However, it has been shown that even flow in medium-sized vessels of healthy volunteers can present more complex flow with secondary patterns such as helical flow (21). In larger arteries or in the presence of cardiovascular diseases, blood flow can be severely altered and can thus differ even more from an ideal parabolic profile (22–24). In addition, even in the presence of limited secondary flow velocities, the influence on WSS can be important (25). Consequently, the axial component of WSS, which was typically used in most studies, may not be sufficient to fully estimate the impact of the three-directional blood flow on the vessel wall. For complex flow, the vectorial time-resolved WSS needs to be considered.

Previously, in vivo WSS vector measurements at specific points in the aorta and the carotid bifurcation were obtained using simple linear near-wall velocity profile assumptions (26). However, those measurements did not allow the WSS to be computed in complete arterial sections, which to date have only been reported based on in vitro models with idealized boundary conditions (13,14).

Recent reports indicate the potential of 3D CINE phase contrast (PC)-MRI (flow sensitive 4D-MRI) for the detailed visualization of complex flow patterns associated with healthy and pathologic hemodynamics (24,27). The nature of such data sets (three spatial dimensions, three blood flow velocity directions, and time) points to the potential of flow-sensitive 4D MRI to provide detailed quantitative flow and vessel wall parameters with complete vascular coverage.

The purpose of this work was to take full advantage of the three-directional nature of MR data and develop an optimized quantitative analysis method to derive vectorial flow and wall parameters from CINE PC MR data. The data analysis strategy combines Green's theorem and B-spline interpolation with its finite difference property to provide an optimal quantification of several blood flow and vessel wall parameters. Calculation of the local blood flow velocity derivatives on the vessel contour using B-spline interpolation allows a direct estimate of time-resolved segmental WSS vectors to be obtained independently of any global assumptions regarding the flow profile.

To our knowledge, the methods and results presented in this study constitute the first report of in vivo analysis of blood flow parameters and vectorial WSS over complete arterial sections.

To test the accuracy of the proposed quantification strategy, synthetic flow data and error propagation analysis were used to evaluate the influence of spatial resolution and signal-to-noise ratio (SNR). To further investigate the effect of spatial and temporal resolution, a detailed comparison of high-resolution 2D-CINE-PC with lower-resolution 3D-CINE-PC data was performed in 19 healthy volunteers in vivo. The aim was to investigate the performance of our data-processing strategy and its reliability for analyzing CINE-3D-PC data compared with a spatially registered 2D-PC technique.

MATERIALS AND METHODS

Synthetic Data

Synthetic data sets were created using a parabolic flow profile with mean velocity of 0.5 m/s in a vessel of diameter 30 mm. According to Poiseuille's flow equation, this results in a flow volume of 353 mL/s and a homogeneous axial WSS of 0.6 N/m². The initial high-resolution synthetic data set with an isotropic pixel size of 0.15 × 0.15 mm² was reduced in 40 steps in order to evaluate the robustness of the quantification method. Filtering with a MRI point-spread function (point spread due to truncation [28]) simulated an increasing pixel size (i.e., isotropic resolution reduction), and Gaussian filtering represented the effects of increased smoothing. The vessel lumen was manually segmented and identical segmentation contours were used for all levels of resolutions and smoothing.

In Vivo MR Acquisitions

Flow measurements were performed in the thoracic aorta of 19 healthy volunteers (mean age: 23 years; range: 20–34; four females). Data were acquired on a 3T MR system (Magnetom TRIO, Siemens, Germany; G_{max} = 40 mT/m, rise time = 200 μ s, eight-channel receive coil) using an RF-spoiled gradient-echo sequence during free breathing and prospective ECG gating. Respiration control was performed based on combined adaptive *k*-space reordering and navigator gating (27).

Data were acquired with interleaved three-directional velocity encoding at eight 2D planes (*2D-CINE-3dir.PC*) transecting the thoracic aorta, and in a 3D volume (*3D-CINE-3dir.PC*) covering the complete thoracic aorta. The 2D planes were positioned at precise landmark locations along the thoracic aorta as schematically illustrated in Fig. 1 (left). The pulse sequence parameters for both 2D and 3D acquisitions are summarized in Table 1 and correspond to commonly used parameters for 3D blood flow visualization (27). For each cine time frame, the velocity encodings for the four acquisitions (reference and three velocity-sensitive scans) were executed consecutively for one and two *k*-space lines along the phase-encoding direction in 2D and 3D, respectively. This resulted in a temporal resolution of 4TR in 2D and 8TR in 3D. (27). After acquisition, the data were corrected for eddy currents, i.e., correction of the linear phase drift according to the static tissues phase drift (29). In a few cases, velocity aliasing was corrected based on an automatic algorithm and manual screening (30).

In addition, a patient (female, age 48 years) hospitalized in the stroke unit of our institution with acute brain ischemia was examined using the *3D-CINE-3dir.PC* protocol. Atherosclerosis and a complex plaque in the descending aorta were demonstrated by a previously reported high-resolution 3D MRI protocol (31).

The study was approved by the local ethics committee and written informed consent was obtained from all subjects.

Data Analysis

The data-processing strategy is illustrated in Figs. 1 and 2. Analysis planes at eight locations in the thoracic aorta

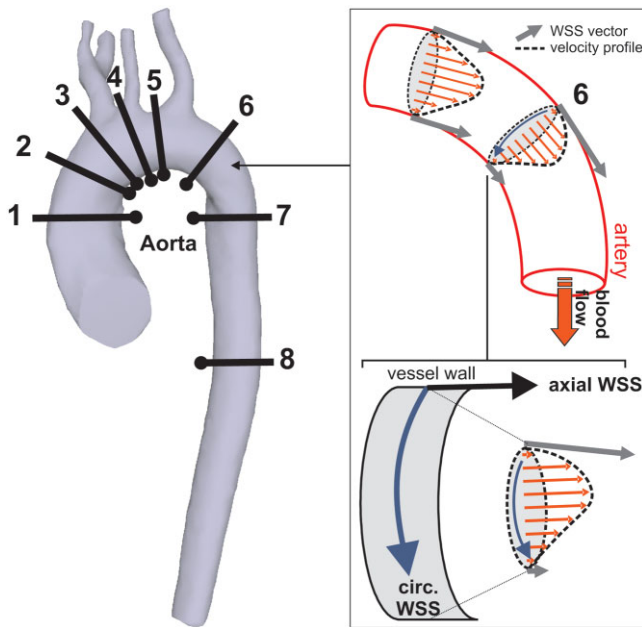


FIG. 1. Schematic illustration of the location of the eight flow analysis planes (left) and the decomposition of the estimated WSS into axial and circumferential components (right). The eight 2D planes are positioned in the ascending aorta (planes 1–3), aortic arch (planes 4 and 5) and the descending aorta (planes 6–8), with the innermost curvature reference positions marked by black dots. WSS estimation is illustrated for the proximal descending aorta (plane 6). Reduced flow along the inner curvature results in asymmetric velocity profiles (dashed lines) and consequently different WSS vectors (gray arrows) at the vessel wall. Note that WSS is a vector quantity and that complex flow, including helical flow components, can induce shear forces along the lumen circumference (circ. WSS) in addition to WSS along the main flow direction (axial WSS). [Color figure can be viewed in the online issue, which is available at www.interscience.wiley.com.]

(Fig. 1, left) were either taken from the image orientation of 2D imaging (*2D-CINE-3dir.PC*, Fig. 2, top left) or retrospectively extracted from the 3D data (*3D-CINE-3dir.PC*, Fig. 2, top right). For *3D-CINE-3dir.PC* analysis planes were extracted within the 3D data volume at the exact location of the 2D imaging planes using 3D visualization software (Ensign, CEI, Apex, NC, USA) (32). The resulting planar magnitude data and three-directional velocities were imported into an in-house analysis tool based on MATLAB (The MathWorks, Natick, MA, USA) that allowed for segmentation and data analysis (33,34). For each data set, several flow and wall parameters were derived: area, flow,

time to peak flow, vectorial WSS, and oscillatory shear index (OSI). In order to compensate for small local fluctuations due to noise, the data were filtered with a Gaussian low-pass filter of fixed radius (1 mm).

Segmentation and Registration

For each CINE time frame the vessel lumen was segmented using cubic B-splines. All segmentation tasks were integrated into a graphical user interface that allowed for interactive frame-wise segmentation by adjusting the position of the interpolating knots, i.e., a finite numbers of points on the contour (Fig. 2, mid). The interpolating knots positions were subsequently used to derive the control points ($c_{x,k}$, $c_{y,k}$) defining the spline. The actual lumen contour ($x(t)$, $y(t)$) and its derivatives ($\dot{x}(t)$, $\dot{y}(t)$) could then be analytically calculated in parametric form (parameter = t) according to the B-spline definition (see Appendix A for details):

$$\begin{cases} x(t) = \sum_{k \in \mathbb{Z}} c_{x,k} \beta^3(t - k) \\ y(t) = \sum_{k \in \mathbb{Z}} c_{y,k} \beta^3(t - k) \end{cases} \quad [1]$$

$$\begin{cases} \dot{x}(t) = \sum_{k \in \mathbb{Z}} c_{x,k} \frac{\partial \beta^3}{\partial t}(t - k) \\ \dot{y}(t) = \sum_{k \in \mathbb{Z}} c_{y,k} \frac{\partial \beta^3}{\partial t}(t - k) \end{cases} \quad [2]$$

Where β^3 is the cubic B-spline basis function of third order, and $\frac{\partial \beta^3}{\partial t}$ represents the cubic differential B-spline basis function of third order.

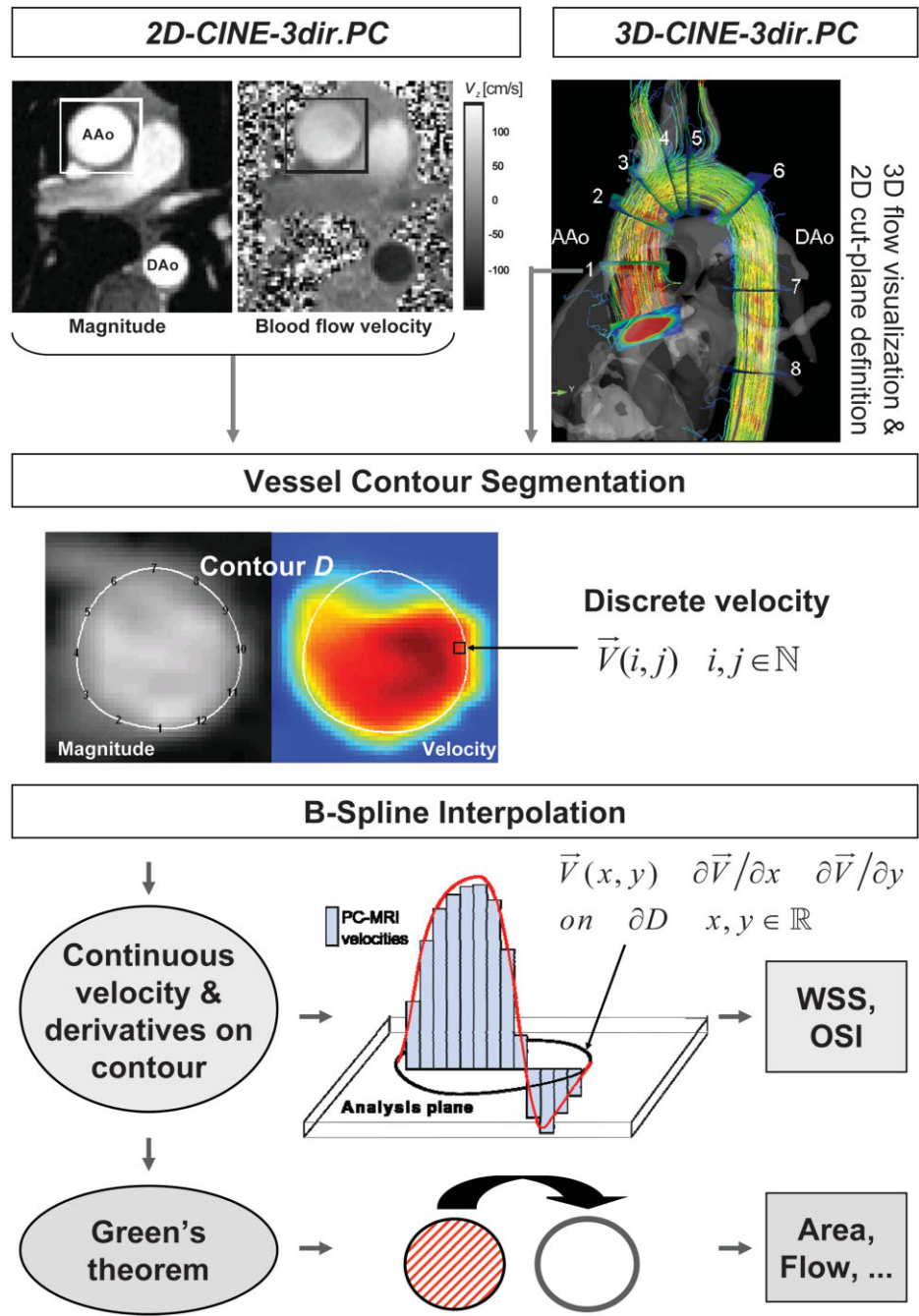
Note that the control points ($c_{x,k}$, $c_{y,k}$) do not belong to the contour and were calculated from the interpolating knots in order to facilitate the segmentation procedure. A fundamental property of B-spline defines $\frac{\partial \beta^3}{\partial t}$ as a finite difference (Eq. [A2]), hence permitting the analytical calculation of Eq. [2].

A reference point corresponding to the inner curvature of the aorta was defined on every contour (black dots on Figs. 1 and 9) in order to allow spatial registration of the WSS vectors between the *2D-CINE-3dir.PC* and *3D-CINE-3dir.PC* acquisitions.

Table 1
Sequence Parameters for In Vivo Acquisitions

	2D-CINE-3dir.PC	3D-CINE-3dir.PC
Voxel size (mm ³) (average between volunteers)	1.24–1.82 × 1.25–1.82 × 5	2.71–2.93 × 1.58–1.69 × 2.60–3.5
Temporal resolution (ms)	4TR = 24.4	8TR = 48.8
v_{enc} (cm/s)	150	150
TE/TR (ms)	3.57/6.1	3.67/6.1
Bandwidth (Hz/pixel)	455	480
α (°)	15	15
Acquisition time (min)	2–5	10–20
Number of time frames	28–40	13–15

FIG. 2. Flow chart representing the flow and wall parameter quantification strategy. **Top:** Planar PC-MRI with three-directional velocity information was either measured directly (2D-CINE-PC-3dir.PC) or retrospectively extracted from volumetric data (3D-CINE-PC-3dir.PC). 3D-CINE-PC-3dir.PC data are visualized as systolic 3D streamlines, i.e., integrations of the velocity field at one instant in time, and include eight interactively positioned 2D analysis planes. **Middle:** Manual segmentation of the lumen contour in magnitude- and color-coded flow velocity images. **Bottom:** To estimate local WSS, B-spline interpolation of the measured discrete velocity data was used to derive continuous flow velocities and velocity derivatives along the segmentation contour. Flow parameters were subsequently calculated by single integration along using Green's theorem. [Color figure can be viewed in the online issue, which is available at www.interscience.wiley.com.]



Interpolation of MR Velocities

To compensate for the limited spatial resolution of the PC MR data, cubic B-spline interpolation was used. Similarly to the B-spline model used for segmentation, the B-spline interpolation model provided continuous velocity and derivatives on the vessel contour. Due to the finite difference property of B-splines, the analytical derivatives, i.e., the local velocity gradient along the segmentation contour ∂D , could be efficiently and easily calculated by using another basis function (Appendix A).

Numerical Computation of WSS

The WSS vector ($\vec{\tau}$) for a Newtonian incompressible fluid can be derived from the velocity field based on the deformation tensor at the vessel wall (Appendix B):

with η : viscosity, \vec{n} : inward unit normal and the deformation tensor:

$$\dot{\epsilon}_{ij} = 1/2(\partial v_i / \partial x_j + \partial v_j / \partial x_i) \quad [4]$$

$\dot{\epsilon}_{ij}$ is directly related to the local velocity derivatives at the vessel lumen, i.e., on the segmentation contour ($i, j = [1, 2, 3] = 3$ orthogonal coordinates, v = velocity components, x = the spatial dimensions).

Calculation of the deformation tensor (Eq. [4]) required the 3D derivation of the velocity vector field. However, assuming transversal 2D analysis planes and no flow

through the vessel wall, Eq. [3] can be simplified to calculate 3D WSS vectors from 2D planes with three-directional velocity fields (Appendix C).

In order to ensure that the estimated WSS vector was tangential to the vessel wall, the projection of $\vec{\tau}$ on the tangential plane was used for the measured WSS (14):

$$\vec{\tau}_{\text{exp}} = \vec{n} \times (\vec{\tau} \times \vec{n}) \quad [5]$$

The WSS vector can be separated into its axial and circumferential components as shown in Fig. 1 (right). In this work we use WSS to denote the magnitude of the WSS vector.

The velocity derivatives $\left(\frac{\partial v_i}{\partial x_j}\right)$ were calculated on the vessel contour using the cubic B-spline interpolation model, which provides first-order analytical derivatives. Equation [5] was evaluated for each CINE time frame with 256 points along the segmented lumen contour. The inward unit normal vector \vec{n} along the lumen contour was analytically calculated from the cubic B-spline contour of the vessel. For each time frame, average WSS vectors were calculated for 12 angular segments along the lumen circumference, starting at the reference point at the inner aortic curvature. A dynamic viscosity η of 4.5 cP was assumed (35).

Numerical Computation of OSI

The OSI represents the temporal oscillation of WSS during the cardiac cycle. It was originally defined by Ku et al. (8) and was further adapted to a general 3D case by He and Ku (36). In this study, the second definition (36) was used:

$$OSI = \frac{1}{2} \left(1 - \frac{|\int_0^T \vec{\tau} \cdot d\vec{t}|}{\int_0^T |\vec{\tau}| \cdot dt} \right) \quad [6]$$

Where T is the duration of the cardiac cycle, and $\vec{\tau}$ is the instantaneous WSS vector.

The OSI in Eq. [6] was numerically computed from the τ after temporal resampling using cubic B-spline temporal interpolation. A 20-fold temporal resampling was found to be sufficient and was used for this study.

Integration Using Green's Theorem

Using Green's theorem (Appendix D), surface integrals can be simplified to contour integrals. This considerably simplifies the practical implementation of 2D integration with interpolation while limiting the computational burden and the numerical error. The lumen contour (∂D , Fig. 2) being defined parametrically by $(x(t), y(t))$, area and flow calculations over the lumen surface D can then be simplified to computing single integrals along ∂D :

$$A = \left| \oint_{\partial D} (x(t)\dot{y}(t) - y(t)\dot{x}(t)) dt \right| \quad [7]$$

$$|Flow| = \left| \oint_{\partial D} P_{v_3}^v(x(t), y(t)) \dot{x}(t) dt \right| \quad [8]$$

with:

$$P_{v_3}^v(x, y) = \int_{-\infty}^y v_3(x, y_N) dy_N \quad [9]$$

where v_3 is the through-plane velocity.

The numerical integration of Eq. [9] was carried out at the original resolution (size N) while Eqs. [7] and [8] were integrated using interpolation on ∂D (size N_i). The computational complexity for the area and flow calculations were thus reduced to $O(N_i)$ and $O(N_i \cdot N)$, respectively, compared to $O(N^2)$ with the same oversampling factor but using a surface integral. $N_i = 256$ was typically used.

Validation

Interobserver and Intermodality Variability

The 2D and 3D data of the first analysis plane of eight volunteers were independently segmented by a second observer, and all derived flow and wall parameters were compared.

Interobserver and intermodality (2D vs. 3D acquisitions) variability was evaluated by calculating relative and absolute errors: $E_{rel} = \frac{2|m1 - m2|}{|m1 + m2|}$ and $E_{abs} = |m1 - m2|$, with $m1$ and $m2$ being the two independent measurements. The errors of the total flow per cardiac cycle and the mean vessel area during one cardiac cycle were assessed based on all analysis planes. The errors of the mean WSS during one cardiac cycle and of the OSI were evaluated based on all analysis planes and all WSS segments.

Error Propagation Analysis

Velocity Data. To evaluate the influence of the SNR of the PC-MRI raw data on the derived flow and wall parameters, a detailed analysis of error propagation was performed. Based on the mean SNR measured in the aorta of all volunteers and all planes, noise in the velocity images was estimated according to (37):

$$\sigma_v = \frac{\sqrt{2}}{\pi} \frac{venc}{SNR} \quad [10]$$

Where SNR is the measured magnitude SNR based on the signal magnitude within the lumen and the background noise, and $venc$ is the velocity sensitivity.

B-Spline Interpolation. Based on Eq. [A4], the 1D cubic B-spline derivative kernel produces a propagation of error with a factor:

$$a_{B-spline} = \sqrt{\sum_{k \in \mathbb{Z}} \left(\frac{d\beta_{int}^3}{dx}(x - k) \right)^2} \frac{1}{\Delta l} \quad [11]$$

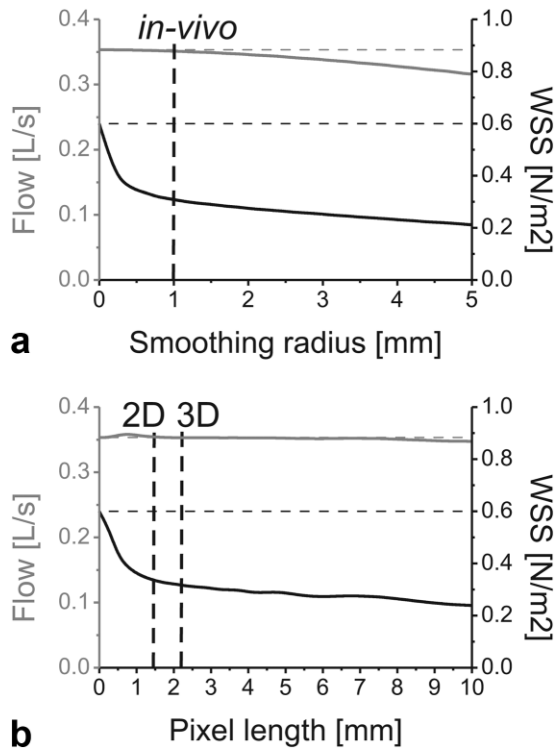


FIG. 3. Effect of Gaussian prefiltering (a) and pixel size (b) on derived flow and WSS for a parabolic synthetic flow profile (mean velocity 0.5 m/s, diameter 30 mm, flow 353 mL/s, WSS 0.6 N/m²). The horizontal lines correspond to the theoretical values of flow and WSS. The prefiltering settings and pixel size used in the volunteer study are indicated by the vertical lines.

Where $\frac{d\beta_{\text{int}}^3}{dx}$ is given by Eq. [A6] and Δl is the sampling period.

Spatiotemporal Averaging. Finally, spatial and temporal averaging affects the error propagations with factors

$$a_{\text{contour}} = \sqrt{\frac{\Delta l}{\text{circumference}}} \text{ over the lumen contour,}$$

$$a_{\text{lumen}} = \sqrt{\frac{(\Delta l)^2}{\text{area}}} \text{ over the lumen area and } a_{\text{time}}$$

$$= \sqrt{\frac{1}{\text{number of time frames}}} \text{ over the cardiac cycle.}$$

Flow and WSS. The error propagation on the flow volume is given by:

$$\sigma_{\text{flow}} = \text{area} \cdot \sigma_v \cdot a_{\text{lumen}} \cdot a_{\text{time}} \quad [12]$$

Simplifying the B-spline interpolation to one dimension, the error propagation for the WSS averaged over the lumen contour and the cardiac cycle is given by:

$$\sigma_{\text{WSS}} = \mu \cdot \sigma_v \cdot a_{\text{B-spline}} \cdot a_{\text{contour}} \cdot a_{\text{time}} \quad [13]$$

RESULTS

Synthetic Data

The effect of systematically varied spatial resolution and low-pass filtering amplitudes on the calculation of flow

and WSS for synthetic data is shown in Fig. 3. Since low-pass filtering (Fig. 3a) is similar to a decrease in spatial resolution (Fig. 3b), both graphs present very similar shapes. It is evident that the proposed method can calculate the almost exact flow and WSS for ideal conditions, i.e., small voxel size and no smoothing. Low resolution strongly affects WSS, while the total flow remains relatively constant. Even at relatively high resolution, WSS is markedly reduced, e.g., for a voxel length of 1 mm the WSS is reduced to 60% of its original value. For further increasing voxel length, WSS remains more stable and is still above 30% of its original value for a voxel length of 10 mm. In contrast, low-resolution imaging introduces very little flow underestimations. The average pixel length and the smoothing radius used in our study are represented by the dashed vertical lines. A 1-mm smoothing and the resolutions used in this study would limit the WSS estimation to about 50% of its real value.

In Vivo Data

Volunteer Study

Flow quantification in the aorta. Exemplary results of time-resolved blood flow based on 2D- and 3D-PC-MRI and averaged over all 19 volunteers are shown in Fig. 4. The small standard deviations (SDs) reflecting interindividual differences between volunteers indicate the high consistency of normal blood flow in young normal subjects. This is coherent with peak aortic velocities previously reported in healthy volunteers (24). As expected, flow quantification based on 3D data slightly underestimated peak systolic and early diastolic retrograde flow. Nevertheless, the flow quantification over all volunteers demonstrated close agreement between 2D and 3D acquisitions, as summa-

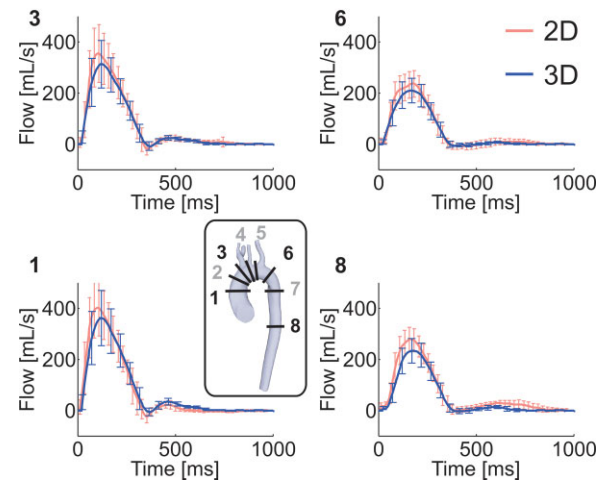


FIG. 4. Average time-resolved volumetric blood flow in the aorta calculated from 2D-CINE-PC-3dir.PC (red) and 3D-CINE-PC-3dir.PC (blue) data for all 19 volunteers. Temporal evolution of blood flow during the cardiac cycle in the ascending aorta (left, planes 1 and 3) and descending aorta (right, planes 6 and 8) demonstrated close agreement between both methods. Note that systolic peak velocities and early diastolic retrograde flow were underestimated for 3D data. The error bars represent the SD over all volunteers. [Color figure can be viewed in the online issue, which is available at www.interscience.wiley.com.]

rized in Table 2. Volumetric blood flow remained constant in the ascending aorta (planes 1–3) and decreased progressively in the aortic arch as blood flowed into the supra-aortic arteries. In the descending aorta (planes 6–8), the flow changes were again limited. The time to peak flow was slightly but systematically overestimated by the 3D data. As a consequence of the compliance of the aorta, the time to peak flow progressively increased along the aorta.

The absolute errors and absolute relative errors between *2D-CINE-3dir.PC* and *3D-CINE-3dir.PC* for all evaluated flow parameters, i.e., the effect of spatiotemporal-resolution on flow quantification, are shown in Table 3 and Fig. 5. The median relative errors of flow and area remained below 18% in 2D and 3D.

WSS estimation in the aorta. For the same analysis planes as in Fig. 4, exemplary results of the estimation of time-resolved WSS magnitude are depicted in Fig. 6, where the individual curves represent WSS magnitude averaged over the lumen contour and over all volunteers. Findings of WSS estimation for all eight analysis planes are summarized in Table 2.

The spatial (Table 2) and temporal (Fig. 6) evolutions of WSS closely agreed between *2D-CINE-3dir.PC* and *3D-CINE-3dir.PC*. However, *3D-CINE-3dir.PC*, based on lower spatiotemporal resolution, systematically underestimated WSS magnitude, as expected from the synthetic data analysis.

The mean WSS magnitude showed a minor increase along the aorta, which correlates well with the evolution of the mean velocity.

Note that the fraction of the circumferential component of the WSS vector was between 10% and 20%, indicating that the vectorial nature of WSS has to be taken into account to fully characterize the wall shear forces. Processing of 3D data generally resulted in larger circumferential WSS components compared to 2D. Finally, the average OSI over all volunteers and WSS segments remained small (5–9%) for all analysis planes and was slightly higher for the 3D data.

The median relative errors for WSS and OSI were within 45 and 65%, respectively (Fig. 5). The absolute error of OSI remained limited at about 5% (Table 3). Those errors are larger than the error predicted from the synthetic data.

Figure 7 shows the local evolution of WSS averaged over all volunteers as a function of analysis plane location, i.e., distribution along the thoracic aorta. The SDs between volunteers, as represented by the error bars, remained relatively small for both 2D and 3D data. Axial WSS and WSS magnitude estimated from the 2D acquisition increased slowly in the ascending aorta (planes 1–3), decreased near the supra-aortic branches in the aortic arch (planes 4 and 5), and eventually increased again in the descending aorta (planes 6–8). Axial and magnitude WSS estimated from the 3D acquisition presented less variations, but the WSS increase in the descending aorta is clearly recognizable. Quantitatively, axial and magnitude WSS, as calculated from the 3D data, were underestimated in comparison to the 2D data.

The average circumferential WSS over all volunteers was positive (right-handed circumferential component) in

Table 2
In Vivo Quantification of Blood Flow and Vessel Wall Parameters in the Aorta*

	Plane							
	1	2	3	4	5	6	7	8
A: Results from 2D-CINE-3dir.PC data								
Flow (ml/cycle)	74.4 (16.2)	70.2 (14.5)	70.7 (17.6)	51.8 (10.9)	48.7 (10.3)	50.0 (11.1)	61.6 (13.0)	63.8 (10.6)
Area (mm ²)	527 (87.5)	489 (80.4)	454 (95.0)	402 (89.6)	363 (59.0)	311 (60.0)	317 (67.4)	295 (50.4)
Mean velocity (m/s)	0.183 (0.0518)	0.187 (0.0480)	0.203 (0.0503)	0.168 (0.0411)	0.170 (0.0354)	0.211 (0.0563)	0.250 (0.0415)	0.278 (0.0454)
Time to peak (ms)	99.6 (14.9)	100 (10.7)	102 (12.7)	116 (26.2)	122 (32.9)	175 (11.4)	174 (14.8)	166 (14.2)
Mean WSS (N/m ²)	0.431 (0.0823)	0.447 (0.0670)	0.444 (0.0907)	0.385 (0.0824)	0.414 (0.0723)	0.466 (0.0889)	0.530 (0.0851)	0.564 (0.0801)
Circumferential WSS (%)	11.8 (11.1)	15.7 (10.8)	16.2 (9.94)	19.4 (8.09)	18.6 (4.79)	10.9 (6.80)	12.1 (6.86)	14.4 (6.67)
OSI mean (%)	6.55 (3.71)	5.29 (2.41)	5.12 (2.72)	5.94 (3.53)	7.47 (2.99)	7.68 (5.09)	8.42 (3.90)	7.49 (3.53)
B: Results from 3D-CINE-3dir.PC data								
Flow (ml/cycle)	73.9 (18.9)	67.0 (14.2)	63.8 (14.3)	50.8 (11.9)	48.4 (10.1)	44.2 (9.59)	45.4 (11.7)	48.5 (9.17)
Area (mm ²)	506 (59.0)	451 (62.9)	435 (87.5)	368 (61.7)	355 (59.8)	317 (59.9)	300 (64.4)	269 (44.8)
Mean velocity (m/s)	0.224 (0.0575)	0.229 (0.0519)	0.226 (0.0432)	0.207 (0.0324)	0.204 (0.0329)	0.211 (0.0362)	0.228 (0.0414)	0.270 (0.0435)
Time to peak (ms)	119 (12.7)	119 (13.7)	123 (19.1)	130 (24.0)	139 (26.1)	171 (18.8)	174 (22.1)	179 (17.9)
Mean WSS (N/m ²)	0.294 (0.0719)	0.309 (0.0669)	0.306 (0.0564)	0.311 (0.0664)	0.308 (0.0492)	0.308 (0.0526)	0.317 (0.0444)	0.384 (0.0768)
Circumferential WSS (%)	24.4 (7.79)	24.9 (9.26)	23.9 (7.97)	25.4 (7.02)	25.1 (6.78)	25.8 (6.92)	20.1 (8.65)	17.4 (7.07)
OSI mean (%)	7.81 (3.00)	7.61 (2.27)	7.77 (2.45)	9.08 (2.28)	8.56 (2.21)	7.82 (3.08)	8.46 (3.94)	6.11 (2.51)

*All data are presented as average values over 19 volunteers. The standard deviation between volunteers is given in parentheses.

Table 3

Mean Absolute Errors Between 2D-CINE-3dir.PC (2D) and 3D-CINE-3dir.PC (3D) as Well as Between Observers in 2D and 3D*

	2D vs. 3D	Interobserver 2D	Interobserver 3D
Flow (ml/cycle)	8.88 (7.02)	1.61 (1.03)	2.69 (1.86)
Area (mm ²)	36.8 (27.6)	32.3 (16.6)	44.7 (14.2)
Mean velocity (m/s)	0.0387 (0.0311)	0.00423 (0.0037)	0.0053 (0.00285)
Time to peak (ms)	17.7 (13.1)	7.73 (14.1)	7.17 (6.72)
Mean WSS (N/m ²)	0.159 (0.0659)	0.033 (0.0123)	0.0477 (0.0156)
OSI mean (%)	5.04 (2.36)	0.827 (0.324)	2.11 (1.7)

*The standard deviation of the error between volunteers is given in parentheses.

the ascending branch of the aorta and inverted in the descending aorta (left-handed circumferential component). Interestingly, the distribution of circular WSS closely resembled known helical flow patterns in the thoracic aorta, changing from a right-handed helix in the upper aortic arch (planes 1–4) to a left-handed helix in the descending aorta (planes 5–8) (24). The circumferential WSS pattern was similar between the 2D and 3D measurements.

A more detailed analysis of the differences between 2D and 3D WSS estimations is provided in the Bland-Altman plots of the axial and circumferential components for all volunteers and analysis planes in Fig. 7c and d. Axial WSS was smaller (on average by 0.078 N/m²) when estimated from 3D data in comparison to 2D data. In contrast, the circumferential WSS did not exhibit a significant systematic bias between 2D and 3D. The 2D-3D difference was smaller and almost symmetric between -0.07 and 0.07 N/m².

Interobserver variability. Figure 8 illustrates the interobserver variability based on repeated processing of the 2D

(Fig. 8a) and 3D (Fig. 8b) data by two independent observers. Overall, variations were moderate, with a median relative interobserver error of approximately 8/17% in 2D/3D. The median interobserver error for OSI was relatively large in proportion (up to 30% relative error in 3D), but the absolute error remained small (up to 2% in 3D, Table 3). The error introduced by lumen segmentation between the two observers was generally higher for the 3D data, i.e., lower resolution, compared to the 2D data at higher spatiotemporal resolution. Flow, area, and WSS showed low median relative error and interquartile distances of the relative error, indicating that the interobserver error was relatively stable between measurements.

Segmental WSS

To illustrate the potential of the presented flow analysis strategy for detailed evaluation of the spatial distribution of WSS, Fig. 9 depicts time-averaged WSS vectors and OSI for one volunteer. Although the major WSS components are axial, the vectorial aspect of WSS is clearly visible. In the ascending aorta (slice 1) and the aortic arch (slice 3), the WSS vectors (green bars) present a substantial right-

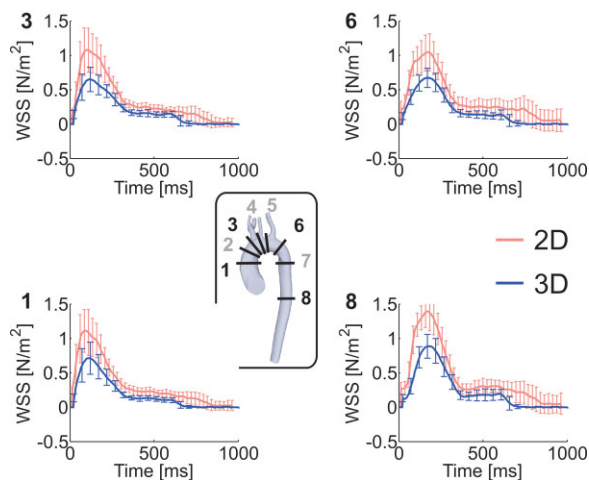


FIG. 5. Distribution of time-resolved average WSS magnitude in the aorta calculated from 2D-CINE-3dir.PC and 3D-CINE-3dir.PC data for all 19 volunteers. Temporal evolution of WSS magnitude during the cardiac cycle in the ascending aorta (left, planes 1 and 3) and descending aorta (right, planes 6 and 8) demonstrated similar shapes but a clear underestimation of WSS estimated from the 3D data. Note that the relatively small error bars represent interindividual variations in WSS and thus indicate the high consistency of the derived WSS data in our group of young healthy volunteers. [Color figure can be viewed in the online issue, which is available at www.interscience.wiley.com.]

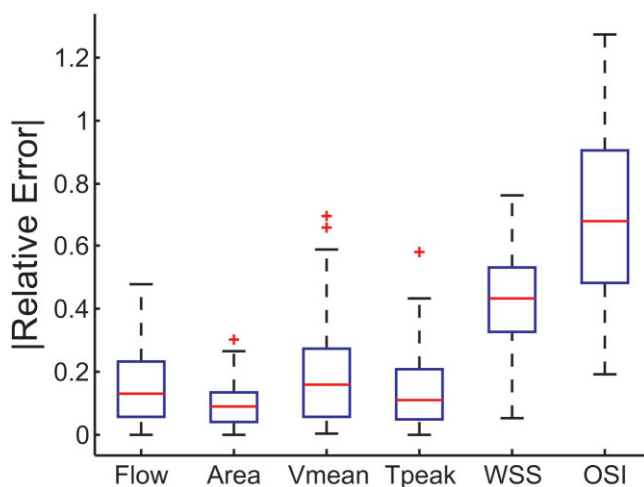


FIG. 6. Box-plot of the absolute value of the intermodality (2D-CINE-3dir.PC vs. 3D-CINE-3dir.PC) relative error for total flow, lumen area, mean velocity, time to peak flow, WSS magnitude, and OSI. The statistics are based on values for all volunteers. Red line = median; blue box = lower and upper quartile values; dashed lines = most extreme values within 1.5 times the interquartile range from the ends of the box; red + sign = outliers, i.e., data with values beyond the ends of the whiskers. [Color figure can be viewed in the online issue, which is available at www.interscience.wiley.com.]

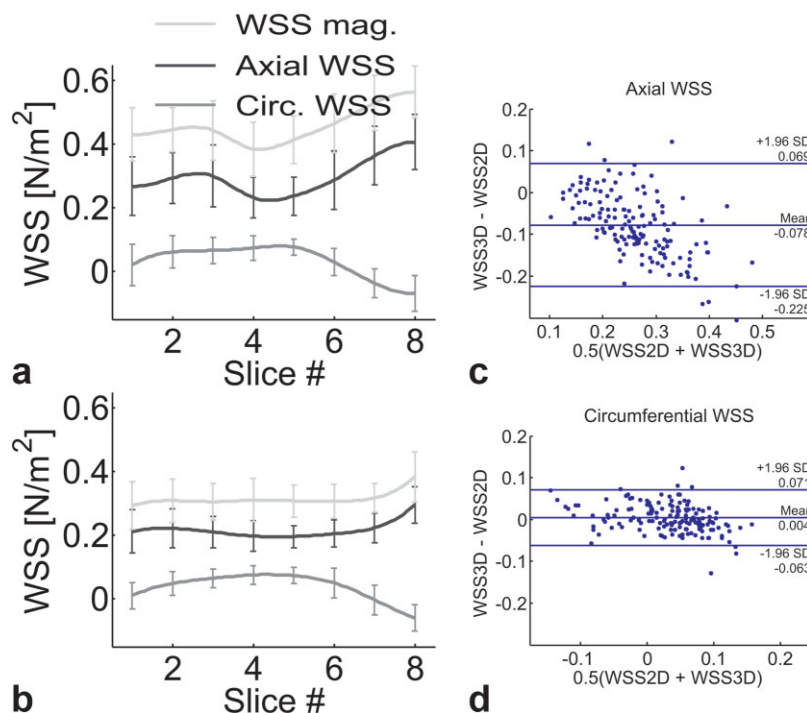


FIG. 7. **a** and **b**: Distribution of temporally averaged WSS components along the thoracic aorta for all volunteers estimated from 2D-CINE-3dir.PC (**a**) and 3D-CINE-3dir.PC (**b**). WSS magnitude, circumferential WSS, and axial WSS were plotted as a function of the slice number, i.e., the location downstream from the aorta according to Fig. 1. The circumferential component of WSS was highest in the aortic arch and closely resembled typical helical flow patterns in the normal aorta. Axial and WSS magnitude were consistently higher for all locations, with a tendency toward higher WSS in the descending aorta. The error bars represent the SD between volunteers. **c** and **d**: Bland-Altman plots for the comparison of results of axial (top) and circumferential (bottom) WSS estimation. The data points represent temporally averaged WSS for 19 volunteers and eight slice locations. [Color figure can be viewed in the online issue, which is available at www.interscience.wiley.com.]

handed circumferential component in combination with higher OSI (magenta bars) on the inner curvature of the aortic arch. In contrast, the WSS vectors in the descending aorta show a left-handed circumferential component. Note that the spatial distribution of WSS vectors from 2D-CINE-3dir.PC and 3D-CINE-3dir.PC is similar, although WSS estimations from 2D-CINE-3dir.PC are slightly larger.

Patient Results

Figure 10 illustrates the application of WSS estimation based on 3D data in a patient with atherosclerosis and an aortic plaque at the inner curvature of the proximal descending aorta. Systolic 3D particle trace visualization (Fig. 10a) showed reduced and potentially locally reversed flow at the plaque location (white arrow), which eventually induced low and inverted WSS vectors as well as increased OSI at this location (Fig. 10b, white arrow). Flow and WSS were considerably different compared to more constant WSS in a normal volunteer, as shown in Fig. 9.

According to the literature, low and oscillating WSS indicate areas that are susceptible to vascular remodeling and thus at risk for progression of atherosclerotic disease (4,7–10). These results therefore indicate the potential of our WSS estimation strategy for analyzing the effects of vascular disease and their impact on the vessel wall.

Error Propagation Analysis

Equation [11] was numerically evaluated and shown to be continuous, periodic, and bound within the following limits:

$$1.18 \leq a_{B-spline} \cdot \Delta l \leq 1.85$$

Average values between volunteers were taken for Δl , area, circumference, SNR, and number of time frames. The average voxel lengths in 2D and 3D were taken for Δl .

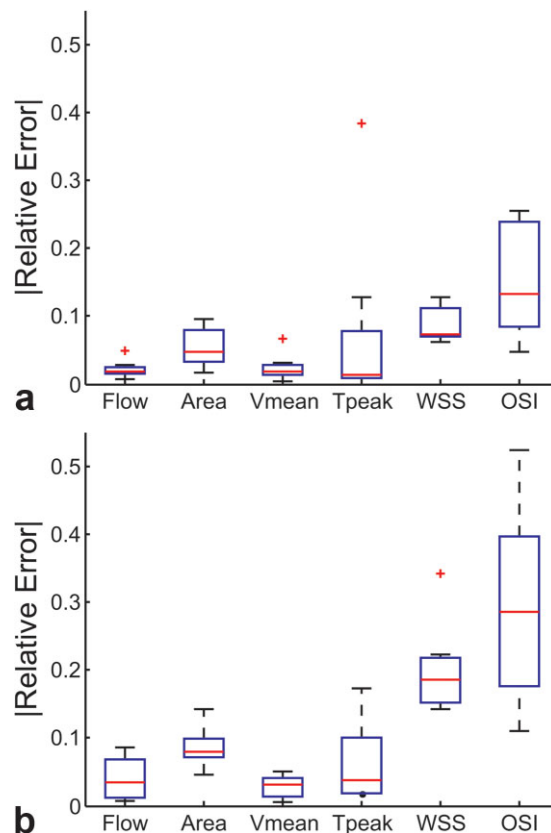


FIG. 8. Boxplots of the absolute value of the interobserver relative error for 2D-CINE-3dir.PC (**a**) and 3D-CINE-3dir.PC (**b**) for total flow, lumen area, mean velocity, time to peak flow, WSS magnitude, and OSI. The statistics are based on values for all volunteers. Red line = median; blue box = lower and upper quartile values; dashed lines = most extreme values within 1.5 times the interquartile range from the ends of the box; red + sign = outliers, i.e., data with values beyond the ends of the whiskers. [Color figure can be viewed in the online issue, which is available at www.interscience.wiley.com.]

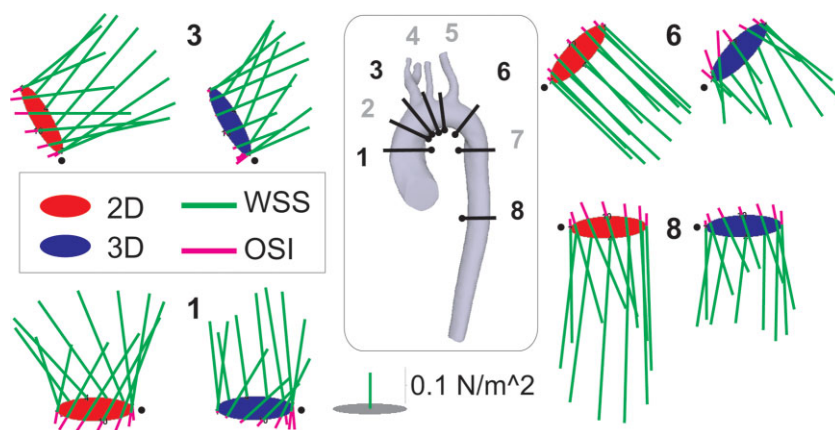


FIG. 9. Segmental distribution of temporally averaged WSS vectors and OSI in the ascending (planes 1 and 3) and descending (planes 6 and 8) aorta for a normal volunteer. WSS and OSI were extracted for 12 segments along the vessel circumference, with the innermost curvature reference positions marked by black dots. For the representation, the OSI for each WSS segment is scaled and opposed to the WSS magnitude, e.g., an OSI of 0.5 would be represented as a bar of the same length as the WSS vector but of opposed direction. For each analysis plane, a direct comparison of WSS vectors (green bars) and OSI (magenta bars) for *2D-CINE-3dir.PC* (red planes) and *3D-CINE-3dir.PC* (blue planes) is shown. Agreement of the segmental WSS and OSI distribution between both data acquisition methods is clearly visible. The expected underestimation of WSS by the lower-resolution 3D data is particularly evident for the high WSS in the descending aorta (plane 8). Note that all planes illustrate the vector nature of WSS and include non-negligible circumferential WSS components.

The results of the error propagation for the velocity, flow, and WSS are presented in Table 4. Flow and WSS errors propagated from measurement errors are about 2 orders of magnitude smaller than the physiologically measured flow and WSS. The propagated errors on flow and WSS were also systematically smaller compared to the intermodality and interobserver errors.

DISCUSSION

Quantification of CINE-PC-MRI data and WSS estimation is a challenging task because of the limited spatiotemporal

resolution, SNR, and the difficulty of accurately segmenting the moving vessel lumens. To date, most approaches have consisted of either fitting a restrictive flow model (e.g., paraboloid method (18)) or deriving numerical flow simulations (11,13,14).

The aim of this study was to evaluate a new processing strategy for the direct estimation of axial and circumferential WSS components and flow parameters from the MR velocity data. The method presented here aims to directly estimate such parameters from PC-MRI data by using cubic B-spline interpolation and Green's theorem. No assumptions other than relative smoothness of the velocity field

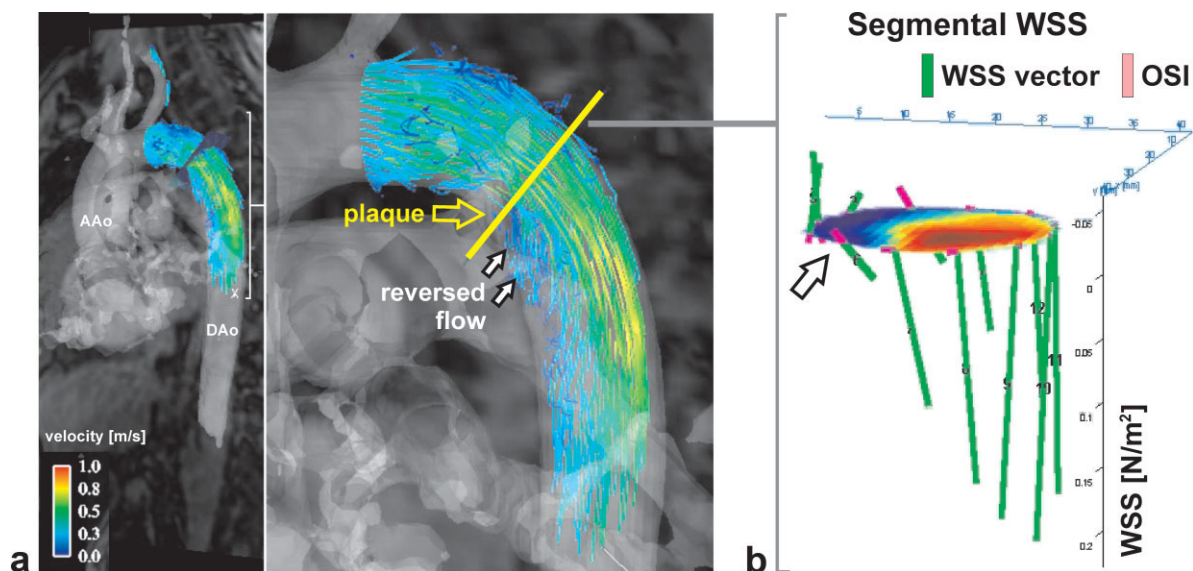


FIG. 10. 3D blood flow visualization and planar quantification in the descending aorta (DAo) of a patient with atherosclerotic disease. Systolic 3D particle traces (a) originating from an emitter plane near the left subclavian artery demonstrate low and potentially reversed flow (white arrows) distal to the location of a previously detected plaque. Flow and wall parameter quantification revealed slow and clearly retrograde flow velocities at the inner curvature, resulting in substantially reduced and even inverted WSS vectors (b, white arrow) at the site of the plaque.

Table 4
Propagation of Measurement Errors

	2D-CINE-3dir.PC	3D-CINE-3dir.PC
SNR	42.9	55.5
σ_v (m/s)	0.0157	0.0122
σ_{flow} (ml/s)	0.0821	0.157
σ_{WSS} (N/m ²)	0.00217	0.00207

(continuity up to the second-order derivatives) were made. B-spline interpolation was chosen based on its excellent interpolation (38,39) quality in combination with its limited computational burden (40–42). Each vessel lumen was segmented using cubic B-spline contour due to its smoothness, flexibility, and continuity properties. Additionally, it has been shown that B-spline of cubic order presents a minimum curvature property (43), which makes it particularly adequate for segmentation of fluid-solid interfaces (44). Furthermore, the finite difference property of the B-spline model provided analytical velocity derivatives along the segmentation contour, which was of particular importance for the calculation of flow parameters and WSS.

Synthetic data analysis showed that the limited resolution provided by MRI introduces underestimation in the measurement of in vivo WSS (about 50% for a WSS of 0.6 N/m²). Flow volume is only slightly underestimated, mainly due to segmentation errors and partial volume effect. The measured WSS is only an estimator of WSS, but remains correlated to the actual WSS.

Error propagation analysis showed that PC-MRI measurement errors have only very limited effects on flow and WSS estimations (two orders of magnitude smaller than the measured parameters).

In vivo data demonstrated close agreement for flow and WSS between 2D- and 3D-CINE-PC. Nevertheless, parameters related to higher spatiotemporal frequencies, such as WSS and OSI, are more limited by the limited resolution of MRI, and 3D-CINE-PC systematically underestimated WSS (relative error of 45%). Note that the relative errors between 2D-CINE-3dir.PC and 3D-CINE-3dir.PC are not only related to the different spatiotemporal resolutions, but are affected by measurement errors or segmentation errors as well, which may explain the higher error level in regard to the predictions from synthetic data. Although WSS values were systematically underestimated in 3D-CINE-3dir.PC, the high consistency between volunteers indicates the potential of WSS estimation for the analysis of relative pathological WSS alterations.

The influence of segmentation error was evaluated by comparing measurements between two independent observers. Flow and area demonstrated small interobserver variability, while the interobserver variability of WSS remained at reasonable levels (7%/18% median relative error in 2D/3D). The overall smaller interobserver variability from the 2D data in comparison to the 3D data can be associated with the higher spatial resolution and improved lumen contrast due to inflow effects. The interobserver variability was assessed using plane 1 in the ascending aorta, which exhibits the most pronounced compliance, i.e., lumen area change, and lumen motion during the

cardiac cycle. Segmentation of this plane was consequently the most complicated, and the resulting interobserver errors should be taken as upper boundaries.

The presence of a circumferential component of aortal WSS accounting for 10–20% of the total WSS indicates that the vectorial nature of WSS has to be taken into account to fully characterize endothelial function. Moreover, circumferential WSS was linked to the normal hemodynamics in the aorta. Right-handed and left-handed helical flow in the ascending and descending branches of the aorta resulted in circumferential WSS reaction forces in the same directions. Interestingly, the intermodality variability between 2D and 3D acquisitions was smaller for the circumferential WSS component than for the WSS magnitude. This may be due to the fact that the smaller circumferential component was derived from velocities with smaller spatial variations. Consequently, it might be better evaluated even at low resolutions (i.e., low sampling frequencies).

A limitation of this study is related to the identical flip angles used for both 2D and 3D acquisitions. Due to the increased blood saturation for 3D imaging by repeated volumetric RF excitation, an individual optimization and lower flip angles may have resulted in improved blood SNR and image quality. Future studies should thus include a more detailed MR protocol optimization of the individual data acquisition methods.

Although interobserver variability and SNR error propagation were analyzed, interscan reproducibility was not evaluated within the framework of this study. Due to the long scan times, repeated measurements were not performed during this study and interscan variability could not be assessed from the available data. However, considering the very limited effect of finite SNR on the measurement error in comparison to the interobserver reproducibility, we speculate that the interobserver variability was the limiting factor regarding reproducibility and thus accounts for most of the interscan variability.

The large intermodality and interobserver relative errors for OSI seem to be due to the low average OSI levels in young healthy volunteers, and are not reflected in the absolute error (below 5%).

Note that although all PC-MRI data underwent eddy-current correction, remaining errors due to concomitant and nonlinear gradients may still introduce errors in the encoded velocities. Since such imperfections substantially increase with increasing distance from the isocenter of the magnet, distal imaging slices, i.e., in the descending aorta, may be most affected. Such errors may have introduced inconsistencies in the flow estimation, as in slices 6-7-8 for the 2D acquisitions or in slices 1-2-3 for the 3D acquisitions. Considering the already long examination protocol of this study, volunteers were not repositioned between 2D-CINE-3dir.PC acquisitions. Further improvements should therefore include corrections for concomitant gradients and gradient field nonlinearity before flow visualization and quantification.

As represented in Table 5, the WSS measurements reported in this study are in good agreement with other published results derived from PC-MRI in the descending and abdominal aorta. Unlike previously reported methods, the method presented here is based on three-directional

Table 5
Reported WSS Values of the Descending and Abdominal Aorta Using MRI*

Study	Aortic branch	Imaging modality	Mean WSS N/m ² (SD)
Stalder et al.	Descending aorta (plane 8) 2D	2D-CINE-3dir.PC	0.56 (0.08)
Stalder et al.	Descending aorta (plane 8) 3D	3D-CINE-3dir.PC	0.38 (0.08)
Wentzel et al. (10)	Descending aorta	2D-CINE-1dir.PC	0.36 (0.17)
Moore et al. (16)	Abdominal aorta suprarenal	2D-CINE-1dir.PC	0.13
Pedersen et al. (17)	Abdominal aorta; Suprarenal/infrarenal	2D-CINE-1dir.PC	0.62/0.27

*Imaging modality is represented as nD -CINE- m dir.PC with n being the imaging dimensionality and m the dimension of the velocity encoding.

velocity encoding in order to derive vectorial WSS. Three-directional velocity encoding and 3D imaging do generate highly valuable additional information compared to 2D techniques; however, they come at the cost of longer scan times. The scan times of 10–20 min for 4D flow-sensitive MRI (3D-CINE-3dir.PC) may limit the clinical application of the method.

Since the presented WSS estimation method is not based on a circular vessel assumption, it can be applied to more irregular vessel areas, such as bifurcations or aneurysms (45). Providing that the velocities measured on a plane transversal to the vessel have sufficient resolution and SNR, the proposed data-processing strategy can provide accurate WSS parameters, such as regional axial and circumferential WSS or OSI.

In highly stenotic regions, however, MRI can no longer be used to image the vessel lumen or a flow profile in the stenosis with sufficient resolution without major methodological modifications. In general, it is not possible to assess correctly the flow if the vessel diameter in the stenosis has the same order of magnitude as the voxel size. Consequently, WSS estimation in stenotic regions is challenging and may suffer from large numerical errors. However, the presented method may still be useful for evaluating stenosis formation as well as pre- and post-stenotic flow (i.e., the flow proximal and distal to the stenosis), and estimating WSS in these regions (46). Such data may provide clinically useful information regarding post-stenotic vessel wall alteration and progression of atherosclerotic disease. More generally, WSS is believed to play an important role in the evolution of atherosclerosis and other arterial diseases, such as aneurysms, for which flow measurements do not present such limitations due to spatial resolution.

Other previously described methods for the estimation of WSS include computational fluid dynamics (CFD). CFD is time-consuming but does not present measurement errors such as those provided by PC-MRI, and can derive very good WSS estimations from the calculated velocity field. However, it remains limited by its assumptions on blood properties, boundary conditions, or vessel wall properties. In addition, CFD-based WSS estimations remain difficult and may require extremely small mesh sizes at the boundary layer of the CFD geometries (15). Nevertheless, CFD has proved to be a useful tool in a number of previous studies (11,13,14). While methods based on PC-MRI are limited because of low spatial resolution and SNR, CFD does not have such restrictions; however, it is limited due to the difficulty of accurately modeling the complex

hemodynamics. In this context, a general comparison of flow analysis between CFD and PC-MRI would be of high interest, but it was beyond the scope of this work. Initial results of an ongoing study at our institution point to the potential of using both PC-MRI and CFD for a mutual enhancement of the quantification accuracy (47).

At present, an exact measurement of WSS in vivo remains a yet-unresolved challenge; however, this study was able to provide the first robust and reproducible in vivo estimation of vectorial WSS in the entire human thoracic aorta.

APPENDIX A

B-Spline Interpolation

Splines are piecewise and smoothly connected polynomials. For B-splines, the spline function is obtained as a sum of a finite number of basis functions. Since each basis function has a finite support, this is a computationally efficient way of representing splines (41–43).

The classical interpolation problem consists in finding $f(x)$ ($x \in \mathbb{R}$) given $f(k)$ ($k \in \mathbb{Z}$), with the interpolating condition that $f(x)|_{x=k_i} = f(k_i)$. The B-spline solution (41–43) is:

$$f(x) = \sum_{k \in \mathbb{Z}} c(k) \beta^n(x - k) \quad [A1]$$

with the B-spline basis function:

$$\beta^n(x) = \underbrace{\beta^0 * \beta^0 * \dots * \beta^0}_{(n+1) \text{ times}}(x)$$

and the coefficients: $c(k) = ((b_1^n)^{-1} * f)(k)$.

Note that $b_1^n(k) := \beta^n(x)|_{x=k}$ can be efficiently calculated using a cascade of first-order recursive filters (40,42). Of particular interest to the topic discussed here is the finite difference property of B-spline:

$$\frac{d\beta^n}{dx}(x) = \beta^{n-1}(x + 1/2) - \beta^{n-1}(x - 1/2) \quad \text{and}$$

$$\frac{df}{dx}(x) = \sum_{k \in \mathbb{Z}} c(k) \frac{d\beta^n}{dx}(x - k) \quad [A2]$$

i.e., the derivative of the spline function is analytically computed by simply using another basis function.

Equations [A1] and [A2] can be rewritten using an interpolating basis function:

$$f(x) = \sum_{k \in \mathbb{Z}} f(k) \beta_{\text{int}}^n(x - k) \quad [\text{A3}]$$

$$\frac{df}{dx}(x) = \sum_{k \in \mathbb{Z}} f(k) \frac{d\beta_{\text{int}}^n}{dx}(x - k) \quad [\text{A4}]$$

With $\beta_{\text{int}}^n = \sum_{k \in \mathbb{Z}} (b)^{-1}(k) \beta(x - k)$
For cubic splines ($N = 3$), we have:

$$\beta_{\text{int}}^3 = \left(\frac{1 - \alpha}{1 + \alpha} \right) \sum_{k \in \mathbb{Z}} \alpha^{|k|} \beta^3(x - k) \quad [\text{A5}]$$

$$\frac{d\beta_{\text{int}}^3}{dx} = \left(\frac{1 - \alpha}{1 + \alpha} \right) \sum_{k \in \mathbb{Z}} \alpha^{|k|} \frac{d\beta^3}{dx}(x - k) \quad [\text{A6}]$$

with $\alpha = -2 + \sqrt{3}$.

APPENDIX B

General Formulation of WSS

The general formulation for the stress tensor is given by (48):

$$\vec{\sigma} = \vec{\tau} + p\vec{I} \quad [\text{A7}]$$

with $\vec{\tau}$: viscous stress tensor, p : pressure, \vec{I} : identity matrix.

While the symmetric second-order stress tensor ($\vec{\sigma}$) depends on the velocity field and the location only, the surface stress vector ($\vec{\sigma}$) additionally depends on the orientation of the vessel wall:

$$\vec{\sigma} = \vec{\sigma} \cdot \vec{n} = \underbrace{\vec{\tau} \cdot \vec{n}}_{\text{viscous stress: } \vec{\tau}} + \underbrace{p\vec{I} \cdot \vec{n}}_{\text{pressure}} \quad [\text{A8}]$$

with \vec{n} : inward unit normal.

For a Newtonian and incompressible fluid, the viscous stress tensor $\vec{\tau}$ is given by $\vec{\tau} = 2\eta\dot{\epsilon}$, with η : viscosity, $\dot{\epsilon}$: deformation tensor (see Eq. [4], Materials and Methods). The general form for the WSS ($\vec{\tau}$) is then

$$\vec{\tau} = 2\eta\dot{\epsilon} \cdot \vec{n} \quad [\text{A9}]$$

Note that if a 1D problem is considered, $\vec{\tau}$ simplifies to: $\vec{\tau}_{1D} = \eta \frac{\partial v}{\partial h}$, with v : the velocity and h : the height of the boundary.

APPENDIX C

Calculation of WSS From 2D Data With 3D Velocity Encoding

The relation between the WSS vector and the three-directional velocity field is given by:

$$\vec{\tau} = 2\eta\dot{\epsilon} \cdot \vec{n}$$

$$= \eta \cdot \begin{pmatrix} 2n_1 \frac{\partial v_1}{\partial x_1} + n_2 \left(\frac{\partial v_1}{\partial x_2} + \frac{\partial v_2}{\partial x_1} \right) + n_3 \left(\frac{\partial v_1}{\partial x_3} + \frac{\partial v_3}{\partial x_1} \right) \\ n_1 \left(\frac{\partial v_1}{\partial x_2} + \frac{\partial v_2}{\partial x_1} \right) + 2n_2 \frac{\partial v_2}{\partial x_2} + n_3 \left(\frac{\partial v_2}{\partial x_3} + \frac{\partial v_3}{\partial x_2} \right) \\ n_1 \left(\frac{\partial v_1}{\partial x_3} + \frac{\partial v_3}{\partial x_1} \right) + n_2 \left(\frac{\partial v_2}{\partial x_3} + \frac{\partial v_3}{\partial x_2} \right) + 2n_3 \frac{\partial v_3}{\partial x_3} \end{pmatrix} \quad [\text{A10}]$$

In order to calculate $\vec{\tau}$ from 2D data with three-directional velocity encoding, it was assumed that the 2D analysis plane was normal to the vessel surface, i.e., $\vec{n} = (n_1, n_2, 0)$. Furthermore, no flow through the vessel condition was enforced, i.e., $\vec{n} \cdot \vec{v} = 0$. This implies: $\vec{n} \cdot \frac{\partial \vec{v}}{\partial x_3} = n_1 \frac{\partial v_1}{\partial x_3} + n_2 \frac{\partial v_2}{\partial x_3} = 0$, and finally, Eq. [A10] reduces to:

$$\vec{\tau} = \eta \cdot \begin{pmatrix} 2n_1 \frac{\partial v_1}{\partial x_1} + n_2 \left(\frac{\partial v_1}{\partial x_2} + \frac{\partial v_2}{\partial x_1} \right) \\ n_1 \left(\frac{\partial v_1}{\partial x_2} + \frac{\partial v_2}{\partial x_1} \right) + 2n_2 \frac{\partial v_2}{\partial x_2} \\ n_1 \frac{\partial v_3}{\partial x_1} + n_2 \frac{\partial v_3}{\partial x_2} \end{pmatrix} \quad [\text{A11}]$$

which can be used to calculate vectorial WSS from data of transversal planes with three-directional velocity information.

APPENDIX D

Green's Theorem

Green's theorem (49) provides the relationship between a surface integral over a regular domain D and a line integral around the simple and oriented closed curve representing the domain boundary (∂D). For a function P continuous in the domain D :

$$\int_{\partial D} P \, dx = - \iint_D \frac{\partial P}{\partial y} \, dx \, dy \quad [\text{A12}]$$

REFERENCES

1. Richter Y, Edelman ER. Cardiology is flow. *Circulation* 2006;113:2679–2682.
2. Nielsen JC, Powell AJ, Gauvreau K, Marcus EN, Prakash A, Geva T. Magnetic resonance imaging predictors of coarctation severity. *Circulation* 2005;111:622–628.
3. Varaprasathan GA, Araoz PA, Higgins CB, Reddy GP. Quantification of flow dynamics in congenital heart disease: applications of velocity-encoded cine MR imaging. *Radiographics* 2002;22:895–905; discussion 905–896.
4. Davies PF. Flow-mediated endothelial mechanotransduction. *Physiol Rev* 1995;75:519–560.
5. Chien S, Li S, Shyy YJ. Effects of mechanical forces on signal transduction and gene expression in endothelial cells. *Hypertension* 1998;31:162–169.
6. De Keulenaer GW, Chappell DC, Ishizaka N, Nerem RM, Alexander RW, Griendling KK. Oscillatory and steady laminar shear stress differentially affect human endothelial redox state: role of a superoxide-producing NADH oxidase. *Circ Res* 1998;82:1094–1101.

7. Cheng C, Tempel D, van Haperen R, van der Baan A, Grosveld F, Daemen MJAP, Krams R, de Crom R. Atherosclerotic lesion size and vulnerability are determined by patterns of fluid shear stress. *Circulation* 2006;113:2744–2753.
8. Ku DN, Giddens DP, Zarins CK, Glagov S. Pulsatile flow and atherosclerosis in the human carotid bifurcation. Positive correlation between plaque location and low oscillating shear stress. *Arteriosclerosis* 1985; 5:293–302.
9. Malek AM, Alper SL, Izumo S. Hemodynamic shear stress and its role in atherosclerosis. *JAMA* 1999;282:2035–2042.
10. Wentzel JJ, Corti R, Fayad ZA, Wisdom P, Macaluso F, Winkelman MO, Fuster V, Badimon JJ. Does shear stress modulate both plaque progression and regression in the thoracic aorta? Human study using serial magnetic resonance imaging. *J Am Coll Cardiol* 2005;45:846–854.
11. Shojima M, Oshima M, Takagi K, Torii R, Hayakawa M, Katada K, Morita A, Kirino T. Magnitude and role of wall shear stress on cerebral aneurysm: computational fluid dynamic study of 20 middle cerebral artery aneurysms. *Stroke* 2004;35:2500–2505.
12. Visser K, Hunink MG. Peripheral arterial disease: gadolinium-enhanced MR angiography versus color-guided duplex US—a meta-analysis. *Radiology* 2000;216:67–77.
13. Kohler U, Marshall I, Robertson MB, Long Q, Xu XY, Hoskins PR. MRI measurement of wall shear stress vectors in bifurcation models and comparison with CFD predictions. *J Magn Reson Imaging* 2001;14:563–573.
14. Papathanasopoulou P, Zhao S, Kohler U, Robertson MB, Long Q, Hoskins P, Xu XY, Marshall I. MRI measurement of time-resolved wall shear stress vectors in a carotid bifurcation model, and comparison with CFD predictions. *J Magn Reson Imaging* 2003;17:153–162.
15. Prakash S, Ethier CR. Requirements for mesh resolution in 3D computational hemodynamics. *J Biomech Eng* 2001;123:134–144.
16. Moore Jr JE, Xu C, Glagov S, Zarins CK, Ku DN. Fluid wall shear stress measurements in a model of the human abdominal aorta: oscillatory behavior and relationship to atherosclerosis. *Atherosclerosis* 1994;110: 225–240.
17. Pedersen EM, Oyre S, Agerbaek M, Kristensen IB, Ringgaard S, Boesiger P, Paaske WP. Distribution of early atherosclerotic lesions in the human abdominal aorta correlates with wall shear stresses measured in vivo. *Eur J Vasc Endovasc Surg* 1999;18:328–333.
18. Oyre S, Ringgaard S, Kozerke S, Paaske WP, Scheidegger MB, Boesiger P, Pedersen EM. Quantitation of circumferential subpixel vessel wall position and wall shear stress by multiple sectored three-dimensional paraboloid modeling of velocity encoded cine MR. *Magn Reson Med* 1998;40:645–655.
19. Box FM, van der Geest RJ, van der Grond J, van Osch MJ, Zwinderman AH, Palm-Meinders IH, Doornbos J, Blauw GJ, van Buchem MA, Reiber JH. Reproducibility of wall shear stress assessment with the paraboloid method in the internal carotid artery with velocity encoded MRI in healthy young individuals. *J Magn Reson Imaging* 2007;26:598–605.
20. Cheng CP, Parker D, Taylor CA. Quantification of wall shear stress in large blood vessels using Lagrangian interpolation functions with cine phase-contrast magnetic resonance imaging. *Ann Biomed Eng* 2002;30: 1020–1032.
21. Wetzel S, Meckel S, Frydrychowicz A, Bonati L, Radue EW, Scheffler K, Hennig J, Markl M. In vivo assessment and visualization of intracranial arterial hemodynamics with flow-sensitized 4D MR imaging at 3T. *AJNR Am J Neuroradiol* 2007;28:433–438.
22. Frydrychowicz A, Schlensak C, Stalder A, Russe M, Siepe M, Beyersdorf F, Langer M, Hennig J, Markl M. Ascending-descending aortic bypass surgery in aortic arch coarctation: four-dimensional magnetic resonance flow analysis. *J Thorac Cardiovasc Surg* 2007;133:260–262.
23. Frydrychowicz A, Harloff A, Jung B, Zaitsev M, Weigang E, Bley TA, Langer M, Hennig J, Markl M. Time-resolved, 3-dimensional magnetic resonance flow analysis at 3 T: visualization of normal and pathological aortic vascular hemodynamics. *J Comput Assist Tomogr* 2007;31:9–15.
24. Kilner PJ, Yang GZ, Mohiaddin RH, Firmin DN, Longmore DB. Helical and retrograde secondary flow patterns in the aortic arch studied by three-directional magnetic resonance velocity mapping. *Circulation* 1993;88:2235–2247.
25. Nerem RM. Vascular fluid mechanics, the arterial wall, and atherosclerosis. *J Biomech Eng* 1992;114:274–282.
26. Tsuji T, Suzuki J, Shimamoto R, Yamazaki T, Nakajima T, Nagai R, Komatsu S, Ohtomo K, Toyo-Oka T, Omata M. Vector analysis of the wall shear rate at the human aortoiliac bifurcation using cine MR velocity mapping. *AJR Am J Radiol* 2002;178:995–999.
27. Markl M, Harloff A, Bley TA, Zaitsev M, Jung B, Weigang E, Langer M, Hennig J, Frydrychowicz A. Time-resolved 3D MR velocity mapping at 3T: improved navigator-gated assessment of vascular anatomy and blood flow. *J Magn Reson Imaging* 2007;25:824–831.
28. Haacke EM, Brown RW, Thompson MR, Venkatesan R. *Magnetic resonance imaging physics: physical principles and sequence design*. New York: Wiley; 1999.
29. Walker PG, Cranney GB, Scheidegger MB, Waseleski G, Pohost GM, Yoganathan AP. Semiautomated method for noise reduction and background phase error correction in MR phase velocity data. *J Magn Reson Imaging* 1993;3:521–530.
30. Bock J, Kreher BW, Hennig J, Markl M. Optimized pre-processing of time-resolved 2D and 3D phase contrast MRI data. In: *Proceedings of 15th Annual Meeting of ISMRM, Berlin, Germany, 2007* (Abstract 3138).
31. Markl M, Dudley P, Frydrychowicz A, Strecker C, Weiller C, Hennig J, Harloff A. Optimized 3D bright blood MRI of aortic plaque at 3 T. *Magn Reson Imaging* 2008;26:330–336.
32. Buonocore MH. Visualizing blood flow patterns using streamlines, arrows, and particle paths. *Magn Reson Med* 1998;40:210–226.
33. Stalder AF, Frydrychowicz A, Canstein C, Hennig J, Markl M. Quantitative planar analysis of flow sensitive 3D CINE MRI. In: *Proceedings of the ISMRM Flow and Motion Study Group Workshop, New York, NY, 2006*.
34. Stalder AF, Frydrychowicz A, Russe MF, Bock J, Hennig J, Markl M. Methodology for optimal quantitative flow analysis by planar analysis of CINE phase contrast 2D or 3D MR data. In: *Proceedings of the 15th Annual Meeting of ISMRM, Berlin, Germany, 2007* (Abstract 3139).
35. Gnasso A, Carallo C, Irace C, Spagnuolo V, De Novara G, Mattioli PL, Pujia A. Association between intima-media thickness and wall shear stress in common carotid arteries in healthy male subjects. *Circulation* 1996;94:3257–3262.
36. He X, Ku DN. Pulsatile flow in the human left coronary artery bifurcation: average conditions. *J Biomech Eng* 1996;118:74–82.
37. Lee AT, Pike GB, Pelc NJ. Three-point phase-contrast velocity measurements with increased velocity-to-noise ratio. *Magn Reson Med* 1995; 33:122–126.
38. Lehmann TM, Gönner C, Spitzer K. Survey: interpolation methods in medical image processing. *IEEE Trans Med Imaging* 1999;18:1049.
39. Lehmann TM, Gönner C, Spitzer K. Addendum: B-spline interpolation in medical image processing. *IEEE Trans Med Imaging* 2001;20:660.
40. Unser M, Aldroubi A, Eden M. Fast B-spline transforms for continuous image representation and interpolation. *IEEE Trans Pattern Anal* 1991; 13:277–285.
41. Unser M, Aldroubi A, Eden M. B-spline signal processing. Part I. Theory. *IEEE Trans Signal Process* 1993;41:821.
42. Unser M, Aldroubi A, Eden M. B-spline signal processing. Part II. Efficient design and applications. *IEEE Trans Signal Process* 1993;41: 834.
43. Unser M. Splines: a perfect fit for signal and image processing. *IEEE Signal Process Magn* 1999;16:22.
44. Stalder AF, Kulik G, Sage D, Barbieri L, Hoffmann P. A snake-based approach to accurate determination of both contact points and contact angles. *Colloids Surf A* 2006;286:92–103.
45. Meckel S, Stalder AF, Santini F, Radu EW, Rufenacht DA, Markl M, Wetzel SG. In vivo visualization and analysis of 3-D hemodynamics in cerebral aneurysms with flow-sensitized 4-D MR imaging at 3 T. *Neuroradiology* 2008;50:473–484.
46. Frydrychowicz A, Berger A, Russe M, Stalder AF, Harloff A, Dittrich S, Hennig J, Langer M, Markl M. Time-resolved MR-angiography and flow-sensitive 4D MRI at 3T for blood flow and wall shear stress analysis in thoracic aortic coarctation. *J Thorac Cardiovasc Surg* 2008; 136:400–407.
47. Stalder AF, Liu Z, Markl M, Hennig J, Korvink J. Patient-specific hemodynamics of the descending aorta: combination of CFD and 4D flow-sensitive MRI. In: *Proceedings of the 16th Annual Meeting of ISMRM, Toronto, Ontario, Canada, 2008*.
48. Emanuel G. *Analytical fluid dynamics*. Boca Raton, FL: CRC Press; 2001 (Abstract 2831).
49. Gustafson GB, Wilcox CH. *Analytical and computational methods of advanced engineering mathematics*. Springer-Verlag, New York. 1998.